Pure appl. geophys. 160 (2003) 555–577
0033 – 4553/03/040555–23

Pure and Applied Geophysics

Radiation from a Finite Reverse Fault in a Half Space

RAÚL MADARIAGA[1]

Abstract — Using a set of well-known results for the seismic field radiated by a simple dip-slip dislocation in a half space, we study interesting details of the motion at the surface of the half space. The static solution for a dislocation in a half space was found by FREUND and BARNETT in 1976. The corresponding elastodynamic solution was solved exactly in the Fourier and Laplace domain by several authors about 20 years ago, however its properties remained unexplored because of analytical difficulties. We remove these difficulties and show that the solution contains three important phenomena: Seismic wave fronts of P, S and SP type; the near-field pulse associated with the propagation of the dislocation front; and the long-time elastic response that converges toward the static solution of Freund and Barnett. Based on these results we show that solutions to all these problems are self-similar and homogeneous in x/h and $\alpha t/h$ so that when the fault depth h approaches 0, the solutions become concentrated near the origin and around the P, S and surface wave travel times. This explains several paradoxes in the radiation from dip-slip faults; among these the most notable are the presence of a point force singularity at the tip of a surface breaking fault and the reduction in high frequency radiation near the surface.

Key words: Earthquakes, elastic wave propagation, dislocations.

1. Introduction

In 1968 Aki published his classical study of the Parkfield earthquake where he computed the near field of strike-slip fault and used this result to accurately fit observed near field displacement on the perpendicular component of station 2 (AKI, 1968). Since then the techniques to compute the near field from strike-slip earthquakes have become increasingly complex and accurate. It is currently common to invert accelerograms for slip distribution and rupture history for large shallow strike-slip earthquakes (see, e.g., ARCHULETA, 1984; WALD and HEATON, 1994; COTTON and CAMPILLO, 1995 or COHEE and BEROZA, 1994). More recently, dynamic models of specific earthquakes have been reported in the literature (OLSEN *et al.*, 1997; PEYRAT *et al.*, 2001).

For shallow dip-slip earthquake, the situation is different because few events of this type have been well recorded in the near field. A substantial effort to model dip-slip events and the strong motion they generate has been made by OGLESBY *et al.*

[1] Ecole Normale Supérieure, 24 rue Lhomond, 75231 Paris Cedex 05, France.
E-mail: madariag@geologie.ens.fr

(1998, 2000a, 2000b), SHI *et al*. (1998). These works raised a number of interesting questions regarding the effect of the free surface above the shallow dipping fault that need careful study. The recent Chichi earthquake of 1999 in Taiwan (see, e.g., KAO and CHEN, 2000) provided a wealth of information that can be used to address a number of questions concerning the effects of the free surface on the strong motion near fault break outs.

In this paper I will review numerous results for kinematic dislocation models that are scattered in the literature in order to clarify a certain number of problems identified by J. Brune (personal communication, 2000). This work will be entirely based on papers published in the late seventies and early eighties by several authors. One of the earliest works on kinematical models of shallow faulting is that of BOORE and ZOBACK (1974) reviewed in chapter 14 of AKI and RICHARDS (1980). The two-dimensional kinematic problem of a dip-slip fault buried in a half space was precisely solved by NIAZI (1975) using the Cagniard-de Hoop method. Unfortunately his solution could not be simply computed. BOUCHON and AKI (1977) and BOUCHON (1978) proposed a numerical spectral method for this problem, nonetheless their discrete frequency wavenumber does not work properly when the fault breaks the free surface due to a singularity of the wavefield at infinite wavenumber. In 1980 I published a different solution to the two-dimensional dip-slip fault in a half space that could be computed exactly using the Cagniard de Hoop method. In the following I will present a shorter derivation of the solution and invert it to space and time domains. I will give exact solutions for ground velocities and the stress component that is different from zero on the free surface. Then I will exploit these solutions to obtain several properties of the effect of the free surface.

2. Basic Formulation

We study the propagation of a dislocation along an inclined straight fault using the Cagniard de Hoop method (AKI and RICHARDS, 1980). We solve the elastic wave equation:

$$\rho \frac{\partial^2 \mathbf{u}}{\partial t^2} = (\lambda + \mu)\nabla(\nabla \cdot \mathbf{u}) + \mu \nabla^2 \mathbf{u} \tag{1}$$

in a half space containing a dislocation source. λ and μ are the elastic constants, ρ is density and elastic wave speeds will be designated α and β for P and S waves, respectively.

As shown in Figure 1, let a dislocation run at speed v along a fault inclined at an angle θ with respect to the horizontal. Rupture starts at position $(0, h)$ and propagates with constant rupture speed v for a finite time L/v in the direction θ stopping at a distance L. Let ξ be a coordinate along the dislocation line. On the fault located between $0 < \xi < L$ slip is constant and equal to D.

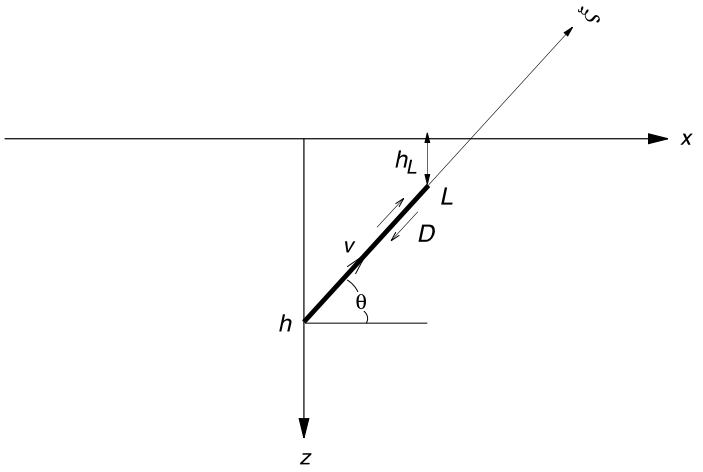

Figure 1
Geometry of a finite fault of dip θ buried in a half space. Rupture starts at the depth h and propagates along the fault for a finite distance L.

Since we are going to use the Cagniard de Hoop method for our calculations we introduce the double Laplace transformed solution defined by

$$u_i(x,z,t) = \frac{1}{2\pi i}\int_{C_s}\frac{1}{2\pi i}\frac{1}{\alpha}\int_{C_p}\bar{u}_i(p,z,s)e^{s(t-\frac{p}{\alpha}x)}\,dp\,s\,ds \tag{2}$$

where C_p and C_s are appropriate Bromwich contours. We note that the convention in (2) is different from that of MADARIAGA (1980). The problem is formally solved by the determination of the doubly transformed displacement $\bar{u}_i(p,z,s)$.

We look for solutions of (1) by the method of potentials. We define as usual $\mathbf{u} = \nabla\phi + \nabla\times(\psi\mathbf{e}_y)$. These potentials satisfy the P- and the S-wave equation, respectively. In order to satisfy appropriate radiation conditions at infinity we choose different forms of the potential in the upper and lower half spaces separated by the line $z = h$, the depth at which the source is located.

$$\bar{\phi} = \Phi^+(s,p)e^{-\frac{s}{\alpha}q_p(z-h)} + \Phi^-(s,p)e^{+\frac{s}{\alpha}q_p(z-h)} \tag{3}$$

$$\bar{\psi} = \Psi^+(s,p)e^{-\frac{s}{\alpha}q_s(z-h)} + \Psi^-(s,p)e^{+\frac{s}{\alpha}q_s(z-h)} \tag{4}$$

where $q_p = \sqrt{1-p^2}$, $q_s = \sqrt{\kappa^2-p^2}$, and $\kappa = \alpha/\beta$, the ratio between P- and S-wave speeds. Signs are chosen so that these fields vanish at infinity. Thus, Φ^+ and Ψ^+ are the appropriate solutions in the half space $z < h$; Φ^- and Ψ^- must be used in $z > h$.

Particle velocities and stresses can be easily computed from (3) and (4) in the Laplace transformed domain. They are written here for reference in a Haskell matrix notation:

$$\begin{bmatrix} \dot{u}_x/\alpha \\ \dot{u}_z/\alpha \\ \sigma_{xz}/\mu \\ \sigma_{zz}/\mu \\ \sigma_{xx}/\mu \end{bmatrix} = \frac{s^2}{\alpha^2} \begin{bmatrix} -p & -q_s & -p & q_s \\ -q_p & p & q_p & p \\ 2pq_p & (\kappa^2-2p^2) & -2pq_p & (\kappa^2-2p^2) \\ (\kappa^2-2p^2) & -2pq_s & (\kappa^2-2p^2) & 2pq_s \\ (\kappa^2-2q_p^2) & 2pq_s & (\kappa^2-2q_p^2) & -2pq_s \end{bmatrix} \begin{bmatrix} \Phi^+ e^{-s/\alpha q_p(z-h)} \\ \Psi^+ e^{-s/\alpha q_s(z-h)} \\ \Phi^- e^{+s/\alpha q_p(z-h)} \\ \Psi^- e^{+s/\alpha q_s(z-h)} \end{bmatrix} . \tag{5}$$

3. Radiation from a Point Dislocation

Let us first provide the solution for the simple problem of a point double-couple source buried in an infinite homogeneous elastic medium. In the following section we will use this solution as a Green function to compute radiation from a finite fault. Let us assume that the source is a point double-couple of Moment M_0 and source time function $H(t)$, where H is Heaviside's function. The point source is located at $(x = 0,\ z = h)$, the dislocation has a dip angle θ and slip is oriented as in Figure 1 so that the fault is a thrust.

We can write the transformed displacement Green function for a point double-couple source in the general form

$$G_i^\ell(p,z,s|0,h,0) = \frac{M_0}{2\mu\kappa^2 s}\mathscr{D}_i^\ell(p)\mathscr{R}^\ell(p,\theta)\frac{e^{-\frac{s}{\alpha}q_\ell(h-z)}}{q_\ell} \quad , \tag{6}$$

where the notation $G_i^\ell(p,z,s|0,h,0)$ indicates that the source is at position $(0,h,0)$ in space-time, and the indices are i, the component of displacement which takes values x or z, and ℓ, which stands for either P or S waves.

$$\mathscr{D}_i^\ell(p) = \begin{bmatrix} -p & q_s \\ q_p & p \end{bmatrix} \tag{7}$$

is the matrix that converts from potential to displacements; and the "plane-wave" radiation patterns $\mathscr{R}^\ell$ are defined by

$$\begin{aligned} \mathscr{R}^p(p,\theta) &= (1-2p^2)\sin 2\theta + 2pq_p\cos 2\theta \\ \mathscr{R}^s(p,\theta) &= 2pq_s\sin 2\theta - (\kappa^2-2p^2)\cos 2\theta \ . \end{aligned} \tag{8}$$

By the same procedure described above for the displacement we can now compute stresses associated with the Green function. Using (5) we get

$$\sigma_{ij}^\ell(p,z,s) = \frac{M_0}{2\kappa^2\alpha}\mathscr{S}_{ij}^\ell(p)\mathscr{R}^\ell(p,\theta)\frac{e^{-\frac{s}{\alpha}q_\ell(h-z)}}{q_\ell} \tag{9}$$

where the coefficients $\mathscr{S}_{ij}^{\ell}$ can be derived from (5):

$$\begin{bmatrix} \mathscr{S}_{xz}^{\ell} \\ \mathscr{S}_{xx}^{\ell zz} \end{bmatrix} = \begin{bmatrix} -2pq_p & (\kappa^2 - 2p^2) \\ (\kappa^2 - 2p^2) & 2pq_s \\ (\kappa^2 - 2q_p^2) & -2pq_s \end{bmatrix} .$$

4. Radiation from a Finite Fault

We consider as in Figure 1 a rupture front starting from the hypocenter at $(x = 0, z = h)$ and propagating along a fault with dip angle θ. At time $t = 0$, rupture starts moving along the fault with constant speed v, and after a certain time $t = L/v$ it stops, leaving a final slip zone of length L. Slip of the fault is uniform and equal to D. As usual, we can compute the radiation from this finite fault by the superposition of point double-couples of type (6).

Let us introduce the coordinate ξ along this line. Then the source located at a point of coordinate ξ along the line will have coordinates $(x = \xi \cos\theta, z = h - \xi \sin\theta)$ and will be activated at time $t = \xi/v$. It will produce a radiation that we can compute from (6):

$$G_i^{\ell}(p, z, s|\xi \cos\theta, h - \xi \sin\theta, \xi/v) = \frac{D}{2\kappa^2 s} \mathscr{D}_i^{\ell}(p) \mathscr{R}^{\ell}(p, \theta) \frac{e^{-\frac{s}{\alpha} q_{\ell}(h-z)}}{q_{\ell}} \times e^{-\frac{s}{\alpha}(\Gamma - p\cos\theta - q_{\ell}\sin\theta)\xi} d\xi \tag{10}$$

where $\Gamma = \alpha/v$ is the ratio between P and rupture speed. In general, for rupture speeds less than the shear-wave speed, $\Gamma > \kappa$. All the other coefficients are independent of ξ.

The radiation from the finite fault is readily computed in the Laplace domain by integration of (10) for a series of identical sources distributed continuously from $(0 \le \xi \le L)$. Carrying out the integration we find that the ground velocity produced by the finite source can be written on the form:

$$\bar{\boldsymbol{u}}_i^{\ell}(p, z, s, L) = \bar{\boldsymbol{u}}_i^{\ell}(p, z, s) - \bar{\boldsymbol{u}}_i^{\ell}(p, z, s) e^{\frac{s}{\alpha}\chi^{\ell}(p,\theta)L} \tag{11}$$

where $\bar{\boldsymbol{u}}_i^{\ell}$ will be defined below, and the factor

$$\chi^{\ell}(p, \theta) = p\cos\theta + q_{\ell}\sin\theta - \Gamma \tag{12}$$

is the directivity due to rupture propagation along the fault.

Each term in (11) represents the radiation from a semi-infinite dislocation that moves along the fault plane with speed v. The velocity field produced by this semi-infinite dislocation is given by:

$$\bar{\boldsymbol{u}}_i^{\ell}(p, z, s) = \frac{\alpha D}{2\kappa^2 s} \frac{\mathscr{D}_i^{\ell}(p) \mathscr{R}^{\ell}(p, \theta)}{\chi^{\ell}(p, \theta)} \frac{e^{-\frac{s}{\alpha} q_{\ell}(h-z)}}{q_{\ell}} \tag{13}$$

and for the stress field we find a similar expression:

$$\bar{\sigma}_{ij}^{\ell}(p,z,s) = \frac{\mu D}{2\kappa^2 s} \frac{\mathscr{S}_{ij}^{\ell}(p)\mathscr{R}^{\ell}(p,\theta)}{\chi^{\ell}(p,\theta)} \frac{e^{-\frac{s}{\nu}q_{\ell}(h-z)}}{q_{\ell}} \tag{14}$$

Equations (13) and (14) represent the waves radiated by a rupture front that starts at the hypocenter and propagates along a fault of dip θ. The rupture front propagates at constant speed v without ever stopping. Behind the rupture front slip is constant and equal to D.

Solution (11) is the sum of a positive rupture front of slip D that starts running at speed v from the hypocenter $(0,h)$ at time $t=0$; and a second dislocation of the opposite sign that is triggered at the instant when the main rupture reaches the end point L of the fault. The appropriate time delay for the second rupture is given by the phase in the exponential term. Computing the effect of finite faults by addition and subtraction of appropriately delayed dislocations is a well-known technique that has been applied to numerous problems, including the computation of finite sources in static and dynamic problems (YOFFE, 1960; COMMINOU and DUNDURS, 1975). This method is exact for uniform slip faults, but it can be used as an approximation for more realistic slip distributions.

4.1 Effect of the Free Surface

The solution we found in the previous section is for a fault line embedded in an infinite medium. The free surface has a very strong effect on this solution; and several authors tried to find approximate expressions for the effect of the surface (BOORE and ZOBACK, 1974; NIELSEN, 1998; OGLESBY *et al.*, 2000a,b). It is very common to assume that the free surface doubles the displacements that would have recorded in a full space. BOUCHON (1998) has given strong support for this approximation. NIELSEN (1998) tried to obtain a similar expression for the only stress component that is not zero on the free surface (σ_{xx}).

Let us consider stress conditions near the free surface. Since both σ_{xz} and σ_{zz} are zero, σ_{xx} can be directly computed from ϵ_{xx} (see also SAVAGE, 1983). On the free surface

$$\epsilon_{zz} = -\frac{\lambda}{\lambda+2\mu}\,\epsilon_{xx} \tag{15}$$

so that

$$\sigma_{xx} = \frac{4\mu(\lambda+\mu)}{\lambda+2\mu}\,\epsilon_{xx} = \frac{2\mu}{1-\nu}\,\epsilon_{xx}\ , \tag{16}$$

where ν is Poisson's modulus. Thus, in general there is little one can say about the horizontal stress on the surface except that the elastic response on the free surface is that of plane stress instead of plane strain.

We can compute the effect of the free surface exactly using the standard seismological method for plane waves. This is a standard problem that need not be repeated here. The effect of the free surface is to multiply the incident fields by a so-called surface response factor. Our final solution on the free surface ($z = 0$) is

$$\bar{\boldsymbol{u}}_i^{\ell}(p,0,s) = \frac{\alpha D}{2\kappa^2 s} \frac{\mathscr{T}_i^{\ell}(p)\mathscr{R}^{\ell}(p,\theta)}{R(p)\chi^{\ell}(p,\theta)} \frac{e^{-\frac{s}{\alpha}q_{\ell}h}}{q_{\ell}} \tag{17}$$

where

$$R(p) = (\kappa^2 - 2p^2)^2 + 4p^2 q_P q_S$$

is Rayleigh's function, and the surface response functions are

$$\mathscr{T}_i^{\ell}(p) = \begin{bmatrix} -4\kappa^2 q_p q_s p & 2\kappa^2(\kappa^2 - 2p^2)q_s \\ 2\kappa^2(\kappa^2 - 2p^2)q_p & 4\kappa^2 p q_P q_s \end{bmatrix} .$$

Expression (17) is the exact solution to our problem in the Laplace transform domain. It can be verified against similar expressions found by BOUCHON (1978) in the Fourier domain using the transformations $s \to i\omega$ and $sp/\alpha \to ik$.

On the free surface the only stress component that is different from zero is σ_{xx} which is given by the relatively complex expression:

$$\bar{\sigma}_{xx}^{\ell}(p,0,s) = \frac{\mu D}{2\kappa^2 s} \frac{S_{xx}^{\ell}(p)\mathscr{R}^{\ell}(p,\theta)}{\chi^{\ell}(p,\theta)} \frac{e^{-\frac{s}{\alpha}q_{\ell}h}}{q_{\ell}} \tag{18}$$

where the surface responses are

$$\begin{aligned} S_{xx}^{P}(p) &= \frac{16(\kappa^2 - 1)p^2 q_p q_s}{R(p)} \\ S_{xx}^{S}(p) &= -\frac{8(\kappa^2 - 1)(\kappa^2 - 2p^2)p q_s}{R(p)} \end{aligned} .$$

These factors are complex in the range $1 < p < \kappa$, become infinite at the Rayleigh pole and become constant at infinity. I consider it very unlikely that a simple relation between stresses with and without free surface may be found.

5. Inversion to the Time Domain

The Laplace transformed solutions (17) and (18) may be inverted to the time and space domain using the Cagniard-de Hoop method. Details of this method are relegated to the Appendix. For running dislocations there are a couple of nontrivial problems with the Cagniard-de Hoop method because the denominators of (17) and (18) have poles in the p complex plane. The residues at these poles must be taken into account in the inversion of either displacements or stresses. There are three poles:

1. A pole at the zero of $R(p)$. This pole is located on the real axis at the Rayleigh wave slowness. It only affects numerical computations when the depth of the hypocenter $h \to 0$.
2. A pole at infinity. This is a very frequent problem with the Cagniard-de Hoop method: the transforms for particle velocities for P and S waves diverge at infinity like p, but their difference converges like p^{-1}. For the stress field the divergence of individual waves is $\mathcal{O}(p^2)$ but the difference converges to a constant value (the residual stress). The main problem created by the pole at infinity is that computations of velocities and stresses for long times become unstable. Convergence can be improved using high precision arithmetic.
3. A pole due to zeroes of the directivity factor, χ^ℓ, in the denominator. This is the most important pole because it is associated with the jump in displacement across the fault. It produces the so-called rupture front wave (see AKI and RICHARDS, 1980). Fortunately, as shown by MADARIAGA (1980), the contribution of the pole at the free surface cancels out if the fault is of finite length L such that it does not break the free surface. If the fault breaks the free surface, both velocities and stresses on the free surface become singular at the exit point of the fault, as will be shown later. For practical numerical computations with a finite sampling interval, the free surface contribution can be computed by letting the fault stop just short of the free surface.

Using the results of the Appendix, we get for the P wave the exact result

$$\dot{u}_i^p(x,0,t) = \frac{\alpha D}{2\pi\kappa^2 r}\Re\left[\frac{\mathcal{T}_i^p(p(t,\phi))\mathcal{R}^p(p(t,\phi),\theta)}{R(p(t,\phi))\chi(p(t,\phi),\theta)}\right]\frac{H(t-r/\alpha)}{\sqrt{\tau^2-1}} \tag{19}$$

and

$$\dot{u}_i^s(x,0,t) = \frac{\alpha D}{2\pi\kappa^2 r}\Re\left[\frac{\mathcal{T}_i^s(p(t,\phi))\mathcal{R}^p(p(t,\phi),\theta)}{R(p(t,\phi))\chi(p(t,\phi),\theta)}\frac{1}{\sqrt{\tau^2-\kappa^2}}\right]H(t-t_{sp}) \tag{20}$$

for S waves. $\Re$ denotes the real part. Here $t_{sp} = \min[r/\beta, |x|/\alpha + \sqrt{1-\kappa^{-2}}h/\beta]$ is the arrival time of the SP wave, the S wave diffracted by the free surface (see BOUCHON, 1978 for a full discussion of the role of this wave in shallow dip-slip faults). Similar expression can be found for the σ_{xx} component of stress. Equations (19) and (20) are the complete solution for a semi-infinite dislocation moving at constant speed along a fault of dip θ. They can be easily computed by any computer algebra package and compared with the same solution when there is no free surface.

A very important property of these solutions is that particle velocity is a homogeneous function of order -1 of the depth h. This means that we can rewrite (19) in the compact form:

$$\dot{u}_i^\ell(x,0,t) = \frac{\alpha D}{h}V_i^\ell\left(\frac{x}{h},\theta,\frac{\alpha t}{h}\right) \tag{21}$$

where the function $V_i^\ell(x/h,\theta,\alpha t/h)$ is homogeneous of order 0; therefore, if we multiply depth h by a certain constant, and the time t and the position x change

proportionally, the velocity increases by a factor of $1/h$. This is a general property of self-similar solutions to the elastic wave equation. It is perhaps important to remark that only self-similar problems can be integrated exactly by the method of Cagniard.

Now we can understand what happens with the radiation from the two ends of the fault. We write the complete time-space solution (11) for the displacement of the free surface due to a fault of length $L < h/\cos\theta$ in the compact form

$$\dot{u}_i^{\ell}(x,0,t,L) = \alpha D\left[\frac{1}{h}V_i^{\ell}\left(\frac{x}{h},\theta,\frac{\alpha t}{h}\right) - \frac{1}{h_L}V_i^{\ell}\left(\frac{x-L\cos\theta}{h_L},\theta,\frac{\alpha(t-L/v)}{h_L}\right)\right] \tag{22}$$

where $h_L = h - L\sin\theta$ is the depth of the second source (see Fig. 2). Thus, the stopping phase due radiation from rupture arrest at L is simply an appropriately scaled and delayed version of the radiation from the starting phase.

In order to show the properties of the velocity field we study a simple model. Since all quantities in (19), (20) and (22) are scaled by depth h, slip D and the P-wave speed α, we choose $h = 1, \alpha = 1$, and $D = 1$. We model a fault of dip $\theta = 30^\circ$ and rupture speed $\Gamma = v/\alpha = 0.4$. The fault length is $L = 1.9$ so that rupture stops just below the free surface at depth $h_L = 0.05$. We choose a finite depth for the end of the fault in order to avoid problems with the singularities due to the Rayleigh wave and the rupture front. The exit point of the fault is $x = 1.732$.

In Figure 3 we show a seismogram section for the horizontal particle velocity produced by the starting phase (the first term in 22). We plot seismograms from $x = 0$ to $x = 3$ every $\Delta x = 0.05$. Figure 4 shows the second term in (22). This represents the contribution from the stopping phase at $L = 1.9$.

In Figure 3 we can easily identify the P and S waves emitted by the initiation of rupture: these are the hyperbolic-shaped arrivals that arrive at the free surface at

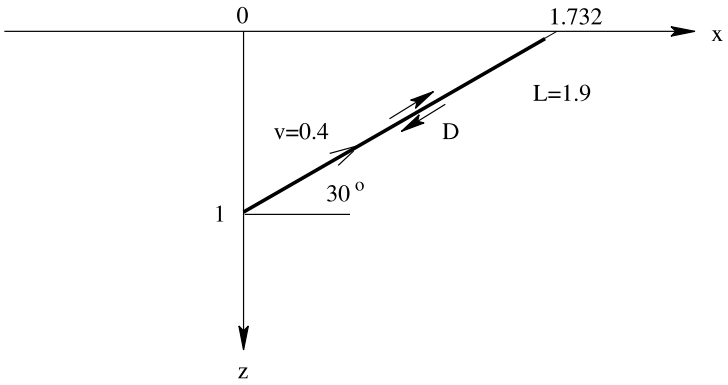

Figure 2
Model used for the simulations. A shallow dipping fault of angle $\theta = 30^\circ$ and length L = 1.9. Rupture start from the hypocenter at time $t = 0$ and propagates at speed $\Gamma = v/\alpha = 0.4$.

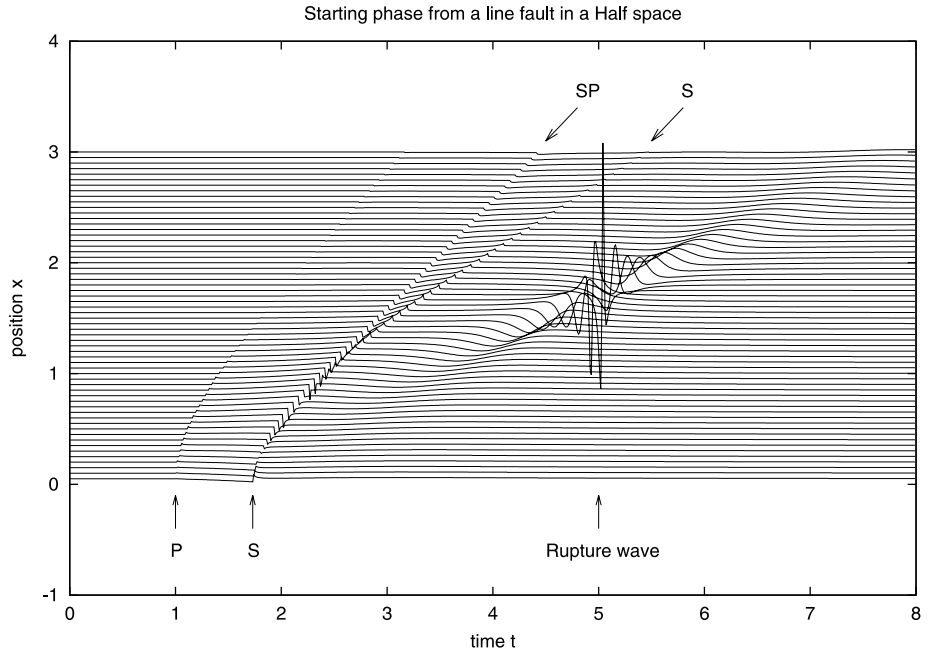

Figure 3
Velocity field produced by the shallow dip-slip dislocation model of Figure 2. This figure shows the starting phases due to the initiation of rupture and its propagation at constant speed along the fault in Figure 2.

point $x = 0$ at times $t = 1$ and $t = 1.73$, respectively. SP waves are also clearly identified in this figure, as the straight lined arrival that splits off the S wave at point $x = 0.707$ and time $t_{sp} = 2.122$. The critical distance for the SP wave can be easily computed from the Vp/Vs ratio κ. The most important arrival in this Figure is the strong rupture phase that appears as the large waves near $x = 1.732,\ t = 2/0.4 = 5$. This is the very well-known rupture front wave associated to the propagating dislocation. The properties of these waves in infinite elastic media were extensively discussed by BOORE and ZOBACK (1974) and AKI and RICHARDS (1980, Chapter 14). We shall study these waves in more detail in a later section.

Figure 4 shows the stopping phases emitted when the dislocation stops at $h_L = 0.9$. These waves were computed using only the second term in (22) except for the minus sign. Although this figure looks very different from the previous one, it is essentially the same as Figure 3 but scaled as indicated in (22). Signals are larger and it is considerably easier to identify the arrivals of P and S waves which decrease slowly as they move away from the tip of the fault. In the forward direction we see a large Rayleigh wave that propagates without geometrical spreading. Behind the Rayleigh wave in the forward direction, we can see the stopping phase of the rupture front wave. This wave has exactly the same shape, phase and arrival time as that shown in Figure 3. As will be discussed in a later section, when we subtract these two

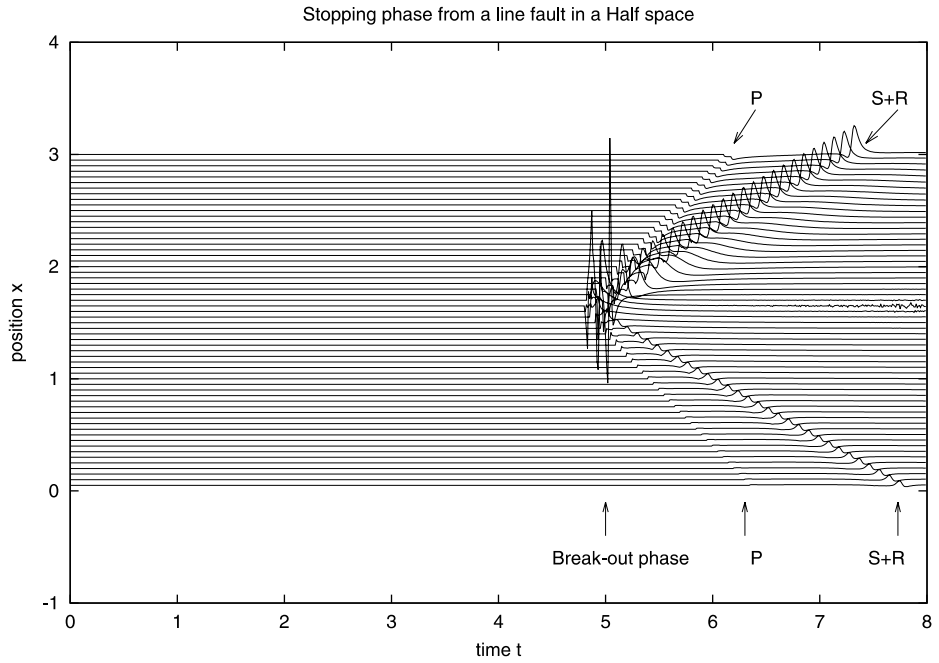

Figure 4
Velocity field produced by the shallow dip-slip dislocation model of Figure 2. This figure shows the stopping (or break-out) phases emitted when the rupture reaches the free surface in Figure 2.

figures to produce the radiation from a finite buried fault, the rupture wave disappears in the forward direction. Some noise is observed in the later part of the seismograms at $x = 1.75$. This is due to the poor numerical canceling of the contribution from P and S waves. These two waves diverge as a function of time, although their sum converges with time as t^{-1}.

As we mentioned earlier, if the rupture reaches the free surface, i.e., if $h_L \to 0$, (19) and (20) can still be used but a number of precautions have to be taken in order to avoid singularities. The Cagniard contour become flat and wraps around the singularities of the Rayleigh wave, the rupture front and the pole at infinity. In this case it is necessary to carefully smooth computations near each of these singularities. In particular, the Cagniard-de Hoop solutions become singular and blow up at $x = 1.73$, this is reasonable since particle velocity is infinite at the point where the fault breaks the surface. The worst instability that occurs when $h_L \to 0$ is due to the poor estimation of the static solution. The small oscillations observed in Figure 4 at $x = 1.75$ become large and the long-time computation blows up. The static solution can be obtained with great difficulty from the Cagniard-de Hoop expressions, however it will be inaccurate and cannot be integrated to displacement without numerical smoothing.

6. Static Displacement and Seismic Moment

As we just showed, retrieving the static solution from the Cagniard contour solutions is a very difficult exercise. The reason is that the solution (17) has been written in terms of separate P and S potentials. It is well known that the separation in potentials fails in the static case. A consequence of this is that the velocity solutions for P and S waves diverge at large time like $O(t)$ and yet their sum decreases at infinity like $O(t^{-1})$. The problem is even more difficult because we would like to obtain displacements by integration of (17). It is much easier to use the solutions found by FREUND and BARNETT (1976) which were used by SAVAGE (1983) to study the seismic cycle in subduction zones. After correcting a few miss-prints in FREUND and BARNETT (1976), we get the following displacements and stresses on the free surface for a line source starting from position $(x = 0, z = h)$

$$
\begin{aligned}
u_x(x,0) &= \frac{D}{\pi}\left[\frac{h(h\sin\theta + x\cos\theta)}{r^2} - \cos\theta \arctan\frac{x}{h}\right] \\
u_z(x,0) &= \frac{D}{\pi}\left[\frac{h(h\cos\theta - x\sin\theta)}{r^2} - \sin\theta \arctan\frac{x}{h}\right] \\
\sigma_{xx}(x,0) &= -\frac{4\mu D}{\pi(1-\nu)}\frac{hx(h\sin\theta + x\cos\theta)}{r^4}
\end{aligned}
\tag{23}
$$

where $r = \sqrt{x^2 + h^2}$ is the distance from the hypocenter to the observation point at $(x, 0)$. The other two components of stress are zero on the free surface.

Once again the displacements in (23) are homogeneous of order 0, i.e., we can write them in the general form

$$u_i(x,0) = DU_i\left(\frac{x}{h}, \theta\right) \ .$$

This solution is self-similar, so that the distribution of displacement along the surface is stretched or compressed depending on the value of h, the depth of the hypocenter. Strictly, solution (23) was computed by Freund and Barnett, for a fault that extends from the hypocenter downward to infinity. They have been used by many authors for a fault that breaks the surface using a particular restriction regarding how the angle $\arctan x/h$ is computed. While this is correct for the computation of displacements, it is inaccurate for stresses as, we show next.

In order to properly compute the displacement and stresses produced by a fault of dip θ and finite length L, we subtract a second dislocation located at the end of the fault $(x = L\cos\theta, z = h_L)$, where $h_L = h - L\cos\theta$:

$$u_x(x,0,L) = D\left[U_x\left(\frac{x}{h}, \theta\right) - U_x\left(\frac{x - L\cos\theta}{h_L}, \theta\right)\right] \ . \tag{24}$$

Because of self-similarity, the effect of the second term is simply a scaled version of the first. We can now see what happens when the fault elongates until it breaks the

free surface, i.e., when $h_L \to 0$. In this case the second term becomes increasingly concentrated in a domain of width h_L around the tip of the fault. When h_L is strictly zero the displacement $U_x((x - L\cos\theta)/h_L) \to \cos\theta H(x - L/\cos\theta)$. This represents a jump of amplitude $\cos\theta$ at the tip of the fault. This term is just the displacement discontinuity at the tip of the surface breaking fault. In previous uses of the FREUND and BARNETT (1976) solution, the second term in (24) has not been explicitly computed because it can be integrated into the definition of the branch cut for the calculation of arctan. For instance, by defining the range $-\pi + \theta < \arctan x/h < \theta$. These two procedures are equivalent but I think that the formulation (24) is clearer.

The stress field near the free surface is computed using the same procedure. We consider first a finite fault of length L and dip θ, then stress field on the free surface $z = 0$ is:

$$\sigma_{xx}(x, 0, L) = \frac{4\mu D}{\pi(1-\nu)}\left[\frac{1}{h}S\left(\frac{x}{h}, \theta\right) - \frac{1}{h_L}S\left(\frac{x - L\cos\theta}{h_L}, \theta\right)\right] \tag{25}$$

where S is the non-dimensional function

$$S(u, \theta) = -\frac{u(\sin\theta + u\cos\theta)}{(u^2+1)^2} \quad . \tag{26}$$

The last term in (25) was not included in the expression for ϵ_{xx} by SAVAGE (1983) because he used the stress field for an infinite fault. If the fault is finite of length L, the second term cannot be neglected. If finite fault breaks the free surface, the second term in (25) becomes zero except near the crack tip, where it is singular. Its value can be computed if we consider stress near the fault tip as a distribution which is the limit of a series of regular functions that depend on the single parameter h_L. We find that

$$\lim_{h_l \to 0} \frac{1}{h_L} S\left(\frac{x - L\cos\theta}{h_L}, \theta\right) = -\frac{\pi}{2}\cos\theta\delta(x - L\cos\theta) \quad . \tag{27}$$

The amplitude of the delta function can be found by integration of (25) from $-\infty$ to ∞ and then letting $h_L \to 0$. Inserting this term into (25), we observe that there is a point force located exactly at the tip of the fault. The strength of the point force is proportional to the jump in displacement across the fault D projected along the surface, multiplied by the plane stress elastic constant $2\mu/(1-\nu)$ (see 16).

Let us now examine the moment tensor representation of a surface-breaking fault. From a straightforward analysis of the way FREUND and BARNETT (1976) found the static solution for a semi-infinite fault, we find, as shown on Figure 5, that displacements and stresses (25) and (24) are due to the combined effect of a finite fault in the lower half space, plus an image fault in the upper virtual half space, and a correction term on the surface. When the fault breaks the surface, as in our example, the set of equivalent forces is that shown in Figure 5. These forces are obviously in equilibrium of force and moment as they should be, otherwise our solution would be mechanically incorrect. Thus the stress singularity of σ_{xx} is crucial to understand the

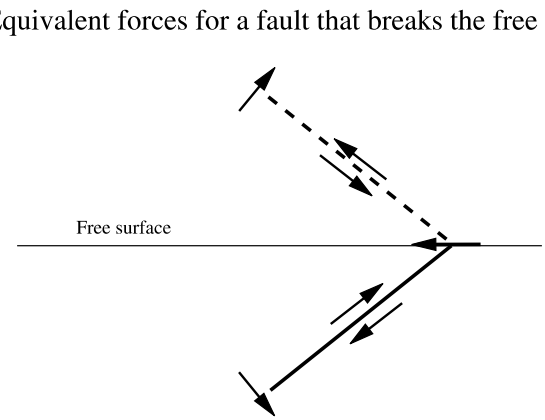

Figure 5
Equivalent forces for a dip-slip fault that breaks the surface.

seismic moment of a surface-breaking fault. Brune (personal communication, 2000) noted that most authors who use equations like (23) to compute the seismic moment have not considered the equilibrium of forces. He was right, most authors did consider the deformation of the fault tip, assuming that since slip is discontinuous there is no force across the fault tip. Most centroid seismic moments are computed using displacement and stress eigenfunctions that satisfy the free surface boundary conditions by construction. Consequently, there is no error in the computation of centroid moment tensors. Errors may appear, however, in the estimation of seismic moments using body waves because in this case the free surface is simulated using reflection coefficients for surface reflected phases. These coefficients fail for very shallow faults; in particular the contribution of the surface-breaking phase is very likely to be in error.

7. The Rupture Pulse around a Propagating Dislocation Front

The effect of the rupture front in the radiation from a dip-slip fault is entirely included in the full solution (22). The rupture front is part of the solution and it occurs whenever the directivity factor $\xi(p(t), \theta) \to 0$. AKI and RICHARDS (1980, chapter 14) studied the rupture front, analyzing the complete solution. It is actually easier to compute the rupture front wave directly from the transformed solution (17).

We notice that (17) has complex poles located at the zeroes of the function $\chi^{\ell}(p, \theta)$ defined by (12), i.e., at

$$p \cos\theta + q_{\ell} \sin\theta = \Gamma \ .$$

Solving for p, we find that the the relevant pole is located at

$$p_p = \Gamma \cos\theta + i\sqrt{\Gamma^2 - c_\ell^2}\sin\theta \tag{28}$$

in the first quadrant of the complex p plane for $0 < \theta < \pi/2$. In the appropriate Riemmann sheet, we get

$$q_\ell = \Gamma \sin\theta - i\sqrt{\Gamma^2 - c_\ell^2}\cos\theta$$

and the derivative

$$\frac{\partial \chi(p)}{\partial p} = -\frac{i\sqrt{\Gamma^2 - c_\ell^2}}{q_\ell} \quad .$$

The contribution of the rupture front is computed using the residue at the pole p_p in (17). After some computations we get

$$\bar{\dot{u}}_i^\ell(x,0,s) = \frac{\alpha D}{2\kappa^2}\Re\left[i\frac{\mathscr{T}_i^\ell(p_p)\mathscr{R}^\ell(p_p,\theta)}{R(p_p)q_\ell \partial\chi^\ell(p_p,\theta)/\partial p}e^{-\frac{s}{\alpha}[p_p x + q_\ell h]}\right] \tag{29}$$

We can transform this expression to the time domain since all the terms are independent of s except the exponential which can be rewritten as

$$e^{-\frac{s}{\alpha}[p_p x + q_\ell h]} = e^{-\frac{s}{\alpha}[\Gamma\xi - i\eta\sqrt{\Gamma^2 - c_\ell^2}]}$$

where ξ and η are the coordinates along the fault and perpendicular to it as shown in Figure 6. We find

$$\bar{\dot{u}}_i^\ell(x,0,t) = \frac{\alpha D}{4\pi\kappa^2}\Re\left[\frac{\mathscr{T}_i^\ell(p_p)\mathscr{R}^\ell(p_p,\theta)}{R(p_p)\sqrt{\Gamma^2 - c_\ell^2}\;\frac{1}{t - \xi/v + i\eta/\alpha\sqrt{\Gamma^2 - c_\ell^2}}}\right] \quad . \tag{30}$$

This is very similar to the rupture wave due to strike-slip faults computed by BOORE and ZOBACK (1974), except that the amplitude is affected by the surface response factor $\mathscr{T}_i^\ell / R(p)$.

After some tedious computations we can show that the radiation patterns become very simple:

$$\begin{aligned} \mathscr{R}^p(p_p,\theta) &= -2i\Gamma\sqrt{\Gamma^2 - 1} \\ \mathscr{R}^s(p_p,\theta) &= (2\Gamma^2 - 1)\kappa^2 \quad . \end{aligned} \tag{31}$$

Expression (30) is the near-field wave produced by a rupture front that starts running at constant speed v from the hypocenter at $(x = 0, z = h)$. In order to compute the radiation from a finite fault that stops at a depth $h_L \to 0$, we have to subtract to expressions like (30) another one that is appropriately retarded in time and space as in (22). It turns out that the rupture front wave and the stopping phase cancel exactly

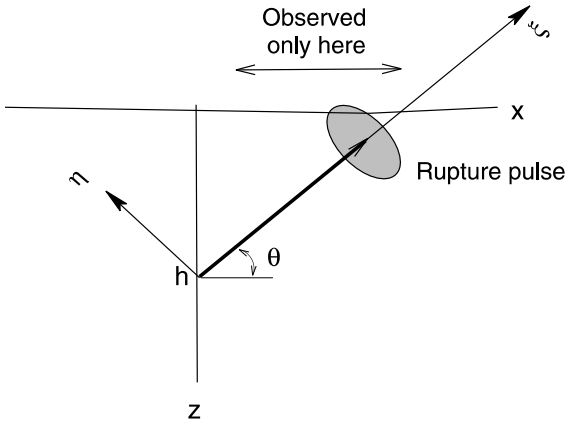

Figure 6
The rupture pulse and the area where it is observed around a dip-slip fault in a half space.

for $\xi > L$, so that the rupture waves can only be observed in the range $0 < \xi < L$. This is quite logical since the rupture wave should only occur in the areas of the fault where rupture propagates. Thus, rupture waves are only observable in the hanging wall; on the foot wall, as seen from Figure 6, $\xi > L$ and there is no rupture front wave.

8. Velocity Field on the Free Surface Due to a Finite Fault

We can now study the velocity field produced by a shallow reverse fault. We consider again the geometry shown in Figure 2. Since these computations are all self-similar, we assumed without loss of generality that depth $h = 1$, P-wave speed $\alpha = 1$ and S-wave speed $\beta = 1/\sqrt{3}$ so that $\kappa = \sqrt{3}$. We also assumed that $v = 0.4\alpha$ and $\theta = 30°$. We assume that rupture continued all the way to the free surface so that $L = h/\sin\theta$ and $h_L = 0$. The tip of the fault is at $x = h/\cos\theta$. Slip the rupture front is a step function.

Figure 7 depicts the horizontal component of particle velocities computed using equations (19) and (20). Figure 8 shows the corresponding vertical particle velocities. We observe the presence of both P and S waves radiated from the hypocenter; these are the weak waves that we identify as P0 and S0 in the figures. We also observe a weak surface converted phase SP0 in the forward direction. The seismic waves emitted when the rupture breaks the free surface are labeled P1, S1 and R1. We observe a clear Rayleigh wave in the forward direction just behind the S1 wave. Since the Rayleigh wave speed is very close to that of shear waves it is difficult to separate the two types of wave.

The most important event in both seismic sections is the large rupture front waves observed on the hanging wall from $0.5 < x < 1.73$. Initially at distances less than $x = 1$, the rupture front wave is just a subtle long wave oscillation, however it becomes sharper and stronger as it nears the break point at $x = 1.73$. This is the

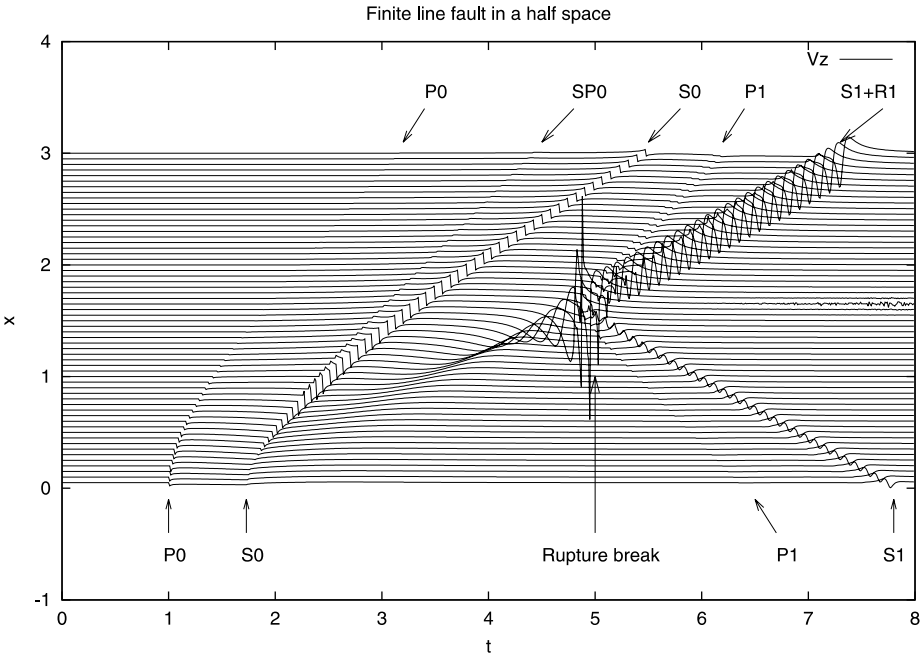

Figure 7
Vertical component of the particle velocity due to a finite fault that stops right below the surface. The arrows identify the phases radiated by the start of rupture (P0, SP0, S0) and from the stopping phase (P1, S1 and R1).

expected behavior of the rupture front waves that are inhomogeneous waves emitted by the rupture front. It is very clear from Figures 7 and 8 that the rupture front wave disappears suddenly for distances beyond the break out point at $x = 1.73$. The reason is that when the rupture front wave reaches the free surface it is exactly canceled by the stopping phase. Thus, there is no rupture front wave in the foot wall. As a consequence, rupture front waves can only be observed above the rupture front. This is the reason why particle velocities are markedly stronger on the hanging wall than in the foot wall. The motion on the foot wall is dominated by the waves radiated from the hypocenter and by the P, S and Rayleigh waves emitted when the rupture breaks the surface (P1, PS1, S1 and R1 in Figures 7 and 8). Of these waves, the most important are the Rayleigh waves radiated in the forward direction as is clearly visible in Figure 4.

It is interesting to compare the result we just obtained for a surface breaking shallow dip-slip fault with a similar solution for a finite dip-slip fault embedded in a homogeneous elastic medium. Particle velocities in this case are given by the same expression as those in a half space, except that the free surface responses $\mathscr{T}_i^\ell / R(p)$ are replaced by $\mathscr{D}_i^\ell$. Figure 9 displays the horizontal component of particle velocities for a finite fault buried in a full space and Figure 10 shows the corresponding vertical

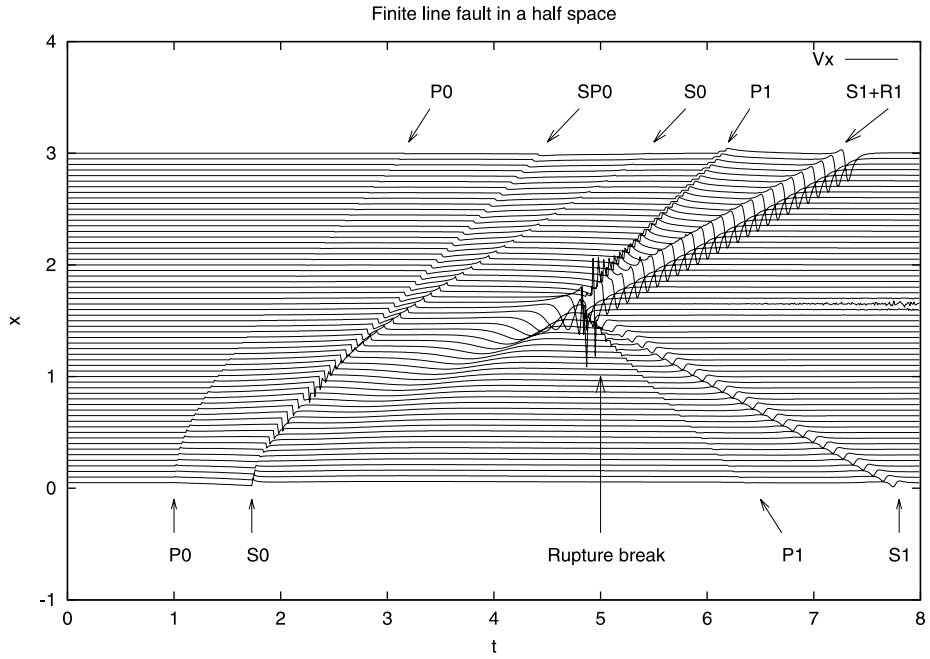

Figure 8
Horizontal component of the particle velocity due to a finite fault that stops right below the surface. The arrows identify the phases radiated by the start of rupture (P0, SP0, S0) and from the stopping phase (P1, S1 and R1).

particle velocities. Numerical computations for a full space are considerably more stable than for a half space at long times. The most obvious difference between figures for half space and full space is the absence of Rayleigh waves in the latter case, as can be clearly observed comparing, for instance, Figures 8 and 10. Amplitude scale in all these Figures is the same so that, as shown by BOUCHON (1978), the amplitudes on the surface of a half space are about the double of those computed in a full space. This is an excellent approximation for the P and S waves emitted by the hypocenter (P0 and S0 in Figs. 7–10). On the other hand, the stopping phases radiated from the surface-breaking event are completely different in a half and a full space. In a half space the wavefield is dominated by the Rayleigh waves emitted in the forward direction. There are also significant differences in the rupture front waves observed clearly in the hanging wall of the fault for a half space, and which are much weaker in the case of a full space. Although the amplitude ratio still approaches 2, the frequency content and the waveforms are very different. Consequently the effect of the free surface can only be approximated by doubling the amplitude far from the hanging wall. Near the fault break out, on the other hand, there seems to be no short cut to accurately computing the full seismograms, including Rayleigh and rupture front waves.

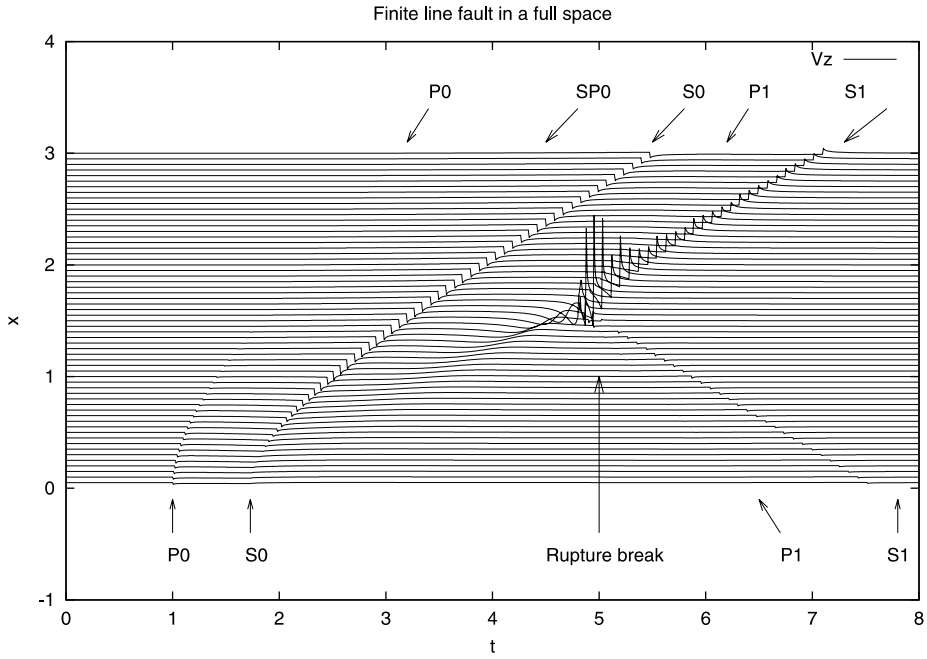

Figure 9
Vertical component of the particle velocity due to a finite fault that stops right below the surface. The arrows identify the phases radiated by the start of rupture (P0, SP0, S0) and from the stopping phase (P1, S1).

9. *Conclusions*

The effect of the free surface on the field created by a rupture front moving along a shallow dip-slip fault can be precisely computed using the Cagniard-de Hoop method. Numerical computations pose a number of problems that we showed were directly related to the singularities of the solution. It seems curious that not all the properties of this simple fault model that was solved in the late 1970s were fully understood. In part this is due to the fact that, although simple looking, the solution (19, 20) has several singularities that have to be carefully studied and smoothed in numerical computations. The most visible singularity is that due to the propagation of the rupture front that produces very large waves in the hanging wall. The other one is the so-called pole at infinity for P and S potentials: the synthetic seismograms for separate P and S waves diverge but the sum converges. This produces inaccuracies in the seismograms computed for long time delays. Careful numerical computations are required to remove these unwanted oscillations. Finally, the Rayleigh waves generated by the break-out of the rupture at the surface are singular on the free surface and, in the two-dimensional model studied here, they do not decay with distance. The only possible

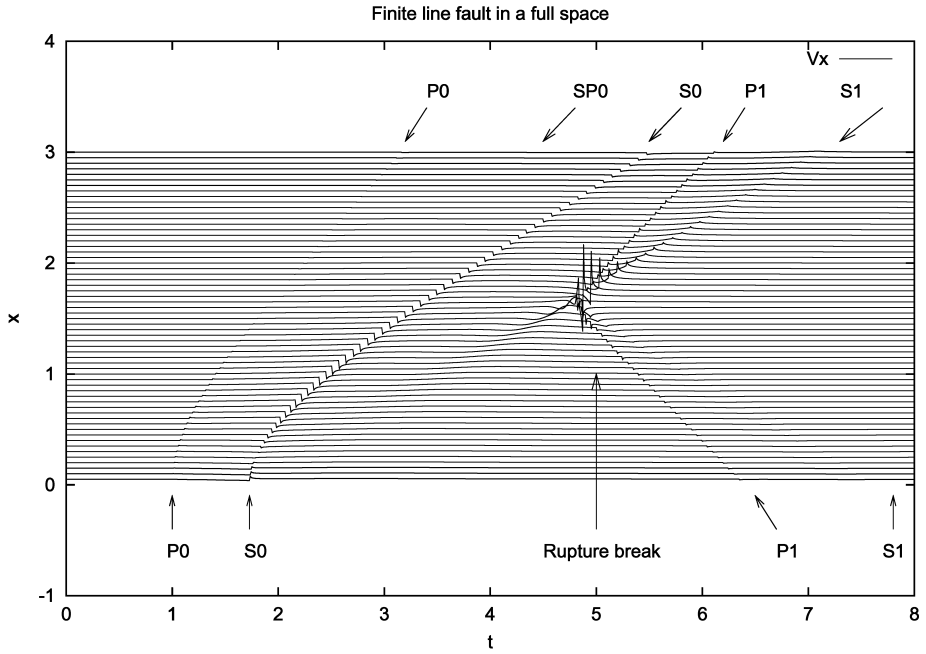

Figure 10
Horizontal component of the particle velocity due to a finite fault that stops right below the surface. The arrows identify the phases radiated by the start of rupture (P0, SP0, S0) and from the stopping phase (P1, S1).

way to write programs that can compute both static and dynamic solutions is to remove or smooth the effect of the singularities, otherwise the computations become unstable and inaccurate. We hope that the results presented in this paper can facilitate the regularization of spectral methods like that of BOUCHON and AKI (1977); they can also be used to test more sophisticated numerical computations by finite differences, finite elements or boundary integral equations. Our results demonstrate that when the rupture breaks the surface the solutions near the break-out point become singular so that the sum of forces and moments remain in equilibrium. Finally, we showed that the rupture front wave—the strong disturbance observed in the vicinity of the rupture front—can only be observed in the hanging wall. On the foot wall it is exactly canceled by the stopping phase emitted when rupture stops at the free surface.

Acknowledgments

I thank K. Aki for his continuous support and encouragement spanning more than 30 years of research. Much of this work was inspired by a seminar given by J. Brune at the Institute of Crustal Studies of the University of California at Santa

Barbara, in July 2000. I thank Dr. Ralph Archuleta for calling my attention to the paper by FREUND and BARNETT (1976). I am most indebted to Dr. Taku Tada who checked the mathematics and found numerous errors. This work began when the author visited ISC during the summer of 2000. Dr. T. Yamashita and Y. Ben-Zion provided very helpful comments. A program to compute synthetic seismograms using the Cagniard-de Hoop method is available on request. I thank the support by CNRS (Centre National de la Recherche Scientifique) under contract 99PNRN13AS of the Programme National de Risques Naturels.

Appendix

Inversion of the Transforms

For a source located at depth $z = h$, we write the expression (17) in the general form

$$\dot{u}_i^\ell(p,z,s) = \frac{\alpha}{2s}\frac{\mathscr{A}_i^\ell(p,\theta)}{q_\ell} e^{-\frac{s}{\alpha}q_\ell h} \tag{32}$$

where $\mathscr{A}_i^\ell(p,\theta)$ is a function of the horizontal slowness p and the dip θ. The right-hand side of (32) is analytic in p, so that the inverse Laplace transform in the space domain (2) can be written as

$$\dot{u}_i^\ell(x,z,s) = \frac{1}{2\pi}\Re\left[\int_0^{i\infty} \frac{\mathscr{A}_i^\ell(p,\theta)}{iq_\ell} e^{-\frac{sp}{\alpha}(p\cos\phi + q_\ell \sin\phi)}\, dp\right] \tag{33}$$

where following Figure 1, we used $x = r\cos\phi$ and $h = r\sin\phi$, with $r = \sqrt{x^2+h^2}$. Expression (33) is a homogeneous function of space and time that can be inverted using the Cagniard-de Hoop method, see, e.g., AKI and RICHARDS (1989) for more details.

As usual we deform the contour of integration from the Imaginary axis to the Cagniard contour defined by the complex valued solution of the equation

$$\tau = p\cos\phi + q_\ell \sin\phi \tag{34}$$

where τ is real parameter.

Solving (34) for p we find the Cagniard contour

$$\begin{aligned} p_\ell &= \tau\cos\phi + i\sqrt{\tau^2 - c_\ell^2}\sin\phi \\ q_\ell &= \tau\sin\phi - i\sqrt{\tau^2 - c_\ell^2}\cos\phi \quad . \end{aligned} \tag{35}$$

For P waves we only take into account the part of the contour for which $\tau > c_p = 1$, while for S waves the contour contains a segment of the real axis in addition to the complex contour. Along the real axis we take $\sqrt{\tau^2 - \kappa^2} = i\sqrt{\kappa^2 - \tau^2}$ so that

$$\begin{aligned} p_\ell &= \tau \cos\phi - \sqrt{\kappa^2 - \tau^2} \sin\phi \\ q_\ell &= \tau \sin\phi + \sqrt{\kappa^2 - \tau^2} \cos\phi \quad . \end{aligned} \tag{36}$$

The Jacobian for the transformation of the integral from the $\Im(p)$ line to the Cagniard contour is

$$\frac{dp}{d\tau} = i \frac{q_\ell}{\sqrt{\tau^2 - c_\ell^2}} \quad .$$

We discuss in the following the time-domain transformation for S waves. For P waves the transform is simpler because there is no headwave. Changing the integration path in (33) to the Cagniard contour we get

$$\dot{\boldsymbol{u}}_i^S(x,z,s) = \frac{1}{2\pi} \Re \left[\int_{\tau_{sp}}^{\infty} \frac{\mathscr{A}_i^S(p,\theta)}{\sqrt{\tau^2 - \kappa^2}} e^{-\frac{sr}{\alpha}\tau} \, d\tau \right] \tag{37}$$

where $\tau_{sp} = \min[\kappa, |\cos\phi| + \sqrt{\kappa^2 - 1}\sin\theta]$ is the arrival time of the PS wave when it precedes the S wave, or the arrival time of the S wave κ if not.

Computing the inverse Laplace transform in time we get

$$\dot{\boldsymbol{u}}_i^S(x,0,t) = \frac{1}{2\pi} \int_1^{\infty} \Re \left[\frac{\mathscr{A}_i^S(p,\theta)}{\sqrt{\tau^2 - \kappa^2}} \right] \delta\left(t - \frac{r}{\alpha}\tau\right) d\tau \tag{38}$$

for $t > r/\alpha$ and 0 otherwise. So that, finally:

$$\dot{\boldsymbol{u}}_i^S(x,0,t) = \frac{\alpha}{2\pi r} \Re \left[\frac{\mathscr{A}_i^S(p(t,\theta))}{\sqrt{\tau^2 - \kappa^2}} \right] H(t - t_{sp}) \quad . \tag{39}$$

This is simply the 2-D Green's function for a double-couple source of any orientation. The same expression is valid for stresses. We must simply replace $\mathscr{A}_i^\ell$ by the appropriate expression extracted from (5).

For the simplicity of numerical computations it is convenient to change variables to $\tau = c_\ell \cosh u$, then $\sqrt{\tau^2 - c_\ell^2} = c_\ell \sinh u$ and all Cagniard contour calculations become very simple.

References

Aki, K. (1968), *Seismic Displacements Near a Fault*, J. Geophys. Res. *73*, 5359–5376.

AKI, K. and RICHARDS, P. G., *Quantitative Seismology: Theory and Methods*, vol. II (W.H. Freeman and Co. San Francisco. 1980).

ARCHULETA, R. (1984), *A Faulting Model for the 1979 Imperial Valley Earthquake*, J. Geophys. Res. *89*, 4559–4585.

BOORE, D. M. and ZOBACK, M. D. (1974), *Near-field Motions from Kinematic Models of Propagating Faults*, Bull. Seismol. Soc. Am. *64*, 555–570.

BOUCHON, M. and AKI, K. (1977), *Discrete Wave Number Representation of Seismic-source Wavefields*, Bull. Seismol. Soc. Am. *67*, 259–277.

BOUCHON, M. (1978), *The Importance of the Surface or Interface P Wave in Near-Earthquake Studies*, Bull. Seismol. Soc. Am. *68*, 1293–1311.

COHEE, B. and BEROZA, G. (1994), *Slip Distribution of the 1992 Landers Earthquake and its Implications for Earthquake Source Mechanics*, Bull. Seismol. Soc. Am. *84*, 692–712.

COMMINOU, M. and DUNDURS, J. (1975), *The Angular Dislocation in a Half Space*, J. Elasticity *5*, 203–216.

COTTON, F. and CAMPILLO, M. (1995), *Frequency Domain Inversion of Strong Motions: Application to the 1992 Landers Earthquake*, J. Geophys. Res. *100*, 3961–3975.

CROUCH, S. L. (1976), *Solution of Plane Elasticity Problems by the Displacement Discontinuity Method*, Int. J. Numer. Meth. Engin. *10*, 301–343.

FREUND, L. B. and BARNETT, D. M. (1976), *A Two-dimensional Analysis of Surface Deformation due to Dip-slip Faulting*, Bull. Seismol. Soc. Am. *66*, 667–675.

MADARIAGA, R. (1980), *A Finite Two-dimensional Kinematic Fault in a Half Space*, Publ. Inst. Geophys. Pol. Acad. Sc. *A-10*, 33–47.

NIAZI, A. (1975), *An Exact Solution for a Finite, Two-dimensional Moving Dislocation in an Elastic Half Space with Applications to the San Fernando Earthquake of 1971*, Bull. Seismol. Soc. Am. *65*, 1797–1826.

NIELSEN, S. B. (1998), *Free Surface Effects on the Propagation of Dynamic Rupture*, Geophys. Res. Lett. *25*, 125–128.

OGLESBY, D. D., ARCHULETA, R. J., and NIELSEN, S. B. (1998), *Earthquakes on Dipping Faults; the Effects of Broken Symmetry*, Science *280*, 1055–1059.

OGLESBY, D. D., ARCHULETA, R. J., and NIELSEN, S. B. (2000a), *The Three-dimensional Dynamics of Dipping Faults*, Bull. Seismol. Soc. Am. *90*, 13,643–13,653.

OGLESBY, D. D., ARCHULETA, R. J., and NIELSEN, S. B. (2000b), *Dynamics of Dip-slip Faulting; Explorations in Two Dimensions*, J. Geophys. Res. *105*, 13,643–13,653.

OLSEN, K., MADARIAGA, R., and ARCHULETA, R. (1997), *Three-dimensional Dynamic Simulation of the 1992 Landers Earthquake*, Science *278*, 834–838.

PEYRAT, S., OLSEN, K., and MADARIAGA, R. (2002), *Dynamic Modelling of the 1992 Landers Earthquake*, J. Geophys. Res. *106*, 25467–25482.

KAO, H. and CHEN, W.-P. (2000), *The Chi-Chi Earthquake Sequence: Active Out-of-sequence Thrust Faulting in Taiwan*, Science *288*, 2346–2349.

SAVAGE, J. C. (1983), *A Dislocation Model of Strain Accumulation and Release Art a Subduction Zone*, J. Geophys. Res. *88*, 4984–4996.

SHI, B., ANOOSHEPOOR, A., BRUNE, J. N., and ZENG, Y. (1998), *Dynamics of Thrust Faulting: 2D Lattice Model*, Bull. Seismol. Soc. Am. *88*, 1484–1494.

SHIN, T. C., KUO, K. W., LEE, W. H. K., and TENG, T. L. (2000), *A Preliminary Report on the 1999 Chi-Chi (Taiwan) Earthquake*, Seismol. Res. Lett. *71*, 24–30.

WALD, D. and HEATON, T. (1994), *Spatial and Temporal Distribution of Slip for the 1992 Landers, California Earthquake*, Bull. Seismol. Soc. Am. *84*, 668–691.

YOFFE, E. H. (1960), *The Angular Dislocation*, Phil. Mag. *5*, 161–175.

(Received March 1, 2001, accepted May 15, 2001)